

8

Natural Intraseasonal and Interannual Variability

8.1 STUFF HAPPENS

Experience shows that weather forecasts are often inaccurate in predicting where and when precipitation will fall and that they get less accurate as the lead time gets longer. In the 1960s, Edward N. Lorenz used simplified versions of the equations that describe the motion of the atmosphere to show that these equations lead to chaos, and prediction of detailed weather information such as the position of weather fronts is likely to be impossible for lead times of greater than about 2 weeks. This is because small errors in the initial field rapidly grow to dominate the forecast fields. Despite this limitation, the quality of forecasts has increased dramatically over the past several decades, so that 10-day forecasts are now often useful. [Figure 8.1](#) shows the correlations between the predictions of a weather forecast model and the observed anomalies in the height fields over the Northern and Southern hemispheres as a function of time starting in 1980. An anomaly correlation of 1 would be a perfect forecast of the 500 hPa height field, so that 3-day forecasts of the height field are very good indeed, but the accuracy drops very quickly for lead times beyond 5 days. It is also apparent that forecasts in the Northern Hemisphere were much better than those in the Southern Hemisphere in the 1980s and 1990s. In the mid-1990s, the Southern Hemisphere forecasts began to improve faster than those in the Northern Hemisphere so that by 2002 the forecasts in the two hemispheres became about equally good. This is because global satellite data began being used much more effectively to determine the initial state of the weather during the 1990s, and satellite observations are much more important in the more ocean-covered and less-populated Southern Hemisphere, where only about 10% of the human population lives.

Although the details of the weather at any instant of time cannot be predicted more than 2 weeks into the future, no matter how much we improve observation systems and models, we can make useful predictions about

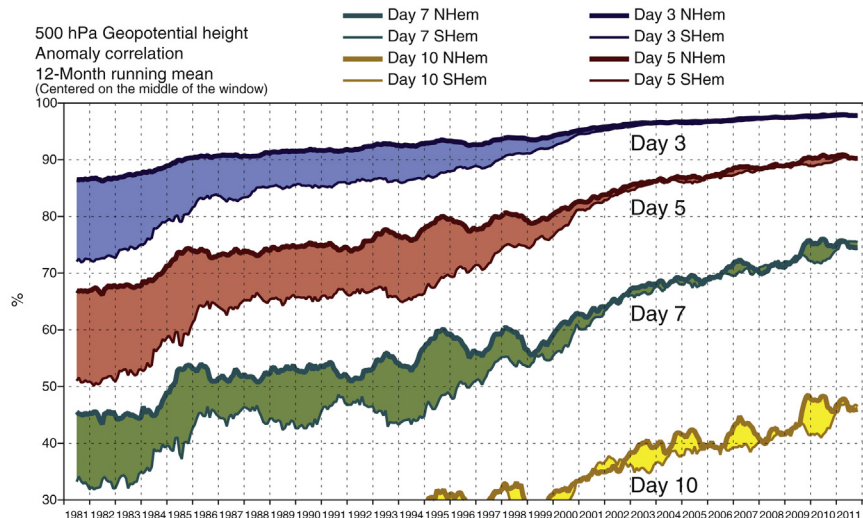


FIGURE 8.1 Quality of weather forecasts as measured by the anomaly correlation of the 500 hPa geopotential height as a function of time from 1981 to 2012 for forecast lead times of 3, 5, 7, and 10 days. Quality estimates are given separately for the Northern and Southern hemispheres, and they converge in about 2002. Courtesy of Martin Janousek, ECMWF.

the statistics of the weather beyond 2 weeks' time. Examples of useful predictions of weather statistics might be the monthly mean temperature during summer, or the probability of an extreme precipitation event in a particular region during a particular season. The possibility to predict the statistics of weather comes from two principle sources. First, the climate system has modes of variability with time scales longer than 2 weeks that may be predictable. If we can predict these low-frequency variations in the natural climate system, then we can make useful predictions about the statistics of weather. Some longer-term predictability may come from the coupling of the ocean to the atmosphere, since the ocean may evolve on longer time scales that are still predictable. Some of these low-frequency modes of variability will be discussed in this chapter. Second, if we know how the climate is being forced, say by greenhouse gas emissions, we can predict how those greenhouse gas emissions will continue into the future. Then, we can make potentially useful predictions of weather statistics a century or more into the future. This is the subject of Chapter 13. Also, from understanding the basic physics of the climate system, we can predict how it will maintain itself differently in a warmer climate, so that the statistics of rainfall intensity, storm intensity, freezing, and drought might be very predictable.

We often distinguish between unforced variability and variability forced by natural or anthropogenic causes. Unforced variability arises

from the internal dynamics without any specific cause. Forced variability can be associated with some change in the boundary conditions of the climate system, such as a volcanic eruption or solar variability on the natural side, or gas or aerosol emissions by human activities on the anthropogenic side. Unforced variability can occur on a variety of time scales from that of a week or two that we normally associate with weather; to intraseasonal variability that might result from internal atmospheric dynamics or interactions between the ocean and the atmosphere; to interannual variability that might result from ocean–atmosphere interactions on time scales of a few years; to natural internal variability that may last up to a thousand years, about the time it takes to turn over the global ocean. Variability that lasts thousands to millions of years may be caused by interactions between variations in Earth’s orbital parameters and its cycles of carbon and ice, and will be discussed in Chapter 12. In this chapter, we will discuss natural variability that has been observed with instrumental climate records, which limits consideration to time scales less than about a decade, if we wish to observe enough events to generalize about them. In Chapter 9, variations on longer time scales that can only be inferred from natural recording systems will be considered.

8.2 INTERNAL ATMOSPHERIC VARIABILITY

The climate system is continuously forced by solar heating of the surface in the tropics, and cooled from the atmosphere and from high latitudes by infrared emission. This heating gradient drives the movement of energy upward in convection and poleward in mid-latitude weather systems or ocean currents. Weather systems and convection events often develop from instabilities of the state toward which the heating gradients drive it, which adds randomness to the variability. The atmosphere and the ocean are relatively weakly damped by frictional dissipation, so that these motions increase in amplitude until they are strongly interacting in a nonlinear way, moving energy from one scale to another. In such a system, energy can be collected in large spatial and temporal scales that are of interest from the perspective of climate. The release of energy on relatively small scales leads ultimately to the great wind and current systems of Earth described in Chapters 6 and 7.

8.2.1 Extratropics: PNA, NAO, and SAM

The atmosphere has a concentration of energy in structures with scales of thousands of kilometers or more that is of interest for weather and climate. Energy is put in at large scales associated with the latitudinal gradient of insolation. The large-scale interactions in mid-latitude weather

systems move energy from the scale at which baroclinic instability generates waves (~ 3000 km) to both larger and smaller scales, with a preference for energy to move toward larger scales and collect there. The energy of the mid-latitude westerly winds is delivered from the smaller scale eddies that define the weather in mid-latitudes. The energetic interactions between mid-latitude storm systems and zonal jets are thus intense, and this translates into modes of variability in which jets and their embedded eddy structures move north and south. One can define these structures as those that best describe the observed variance in a mean-square sense, and this can be done efficiently using what Lorenz called *empirical orthogonal functions* (EOFs). This is an objective mathematical technique that can find spatial patterns in data that explain a disproportionate amount of variance. EOFs are spatial structures that take advantage of the correlations between different locations to explain a lot of variance. If they robustly explain a lot of variance, then we tend to associate them with real modes of variability of the climate system, especially if a physical argument can be given for why such a structure should exist.

To introduce the concepts of space and time scales of mid-latitude atmospheric variability, we can consider the 500 hPa height field. The 500 hPa height field is a useful scalar quantity for characterizing extratropical variability, since the wind and temperature can both be related to the geopotential height through the geostrophic and hydrostatic relations. Since 500 hPa is at the mid-point of the mass of the atmosphere, it captures phenomena that extend through the depth of the troposphere. We can divide its temporal variability by filtering into periods shorter than 7 days, periods between 7 and 30 days, and periods longer than 30 days. The total variance and the variance in each of these categories are shown in Fig. 8.2 for the Northern Hemisphere winter half year (October to March), and in Fig. 8.3 for the Southern Hemisphere winter half year (April to September). Also shown is the climatological height field, the average over all days in the half year and all the years in the sample.

Figure 8.2 shows that the variability of 500 hPa height during Northern Hemisphere winter is highest over the oceans and least in mountainous areas. The variability over the oceans is contributed mostly by phenomena with periods longer than 30 days. Variability on intermediate time scales between 7 and 30 days occurs preferentially on the downstream (eastward) sides of the oceans. The high frequency variability, with time scales less than 7 days, occurs on the westward edges of the oceans – one in the Pacific and one in the Atlantic. The high-frequency eddies evolve into the intermediate-scale eddies as they propagate toward the east. The high frequency variance maxima are associated with the jet streams and their associated storm tracks, as previously discussed in Fig. 6.18.

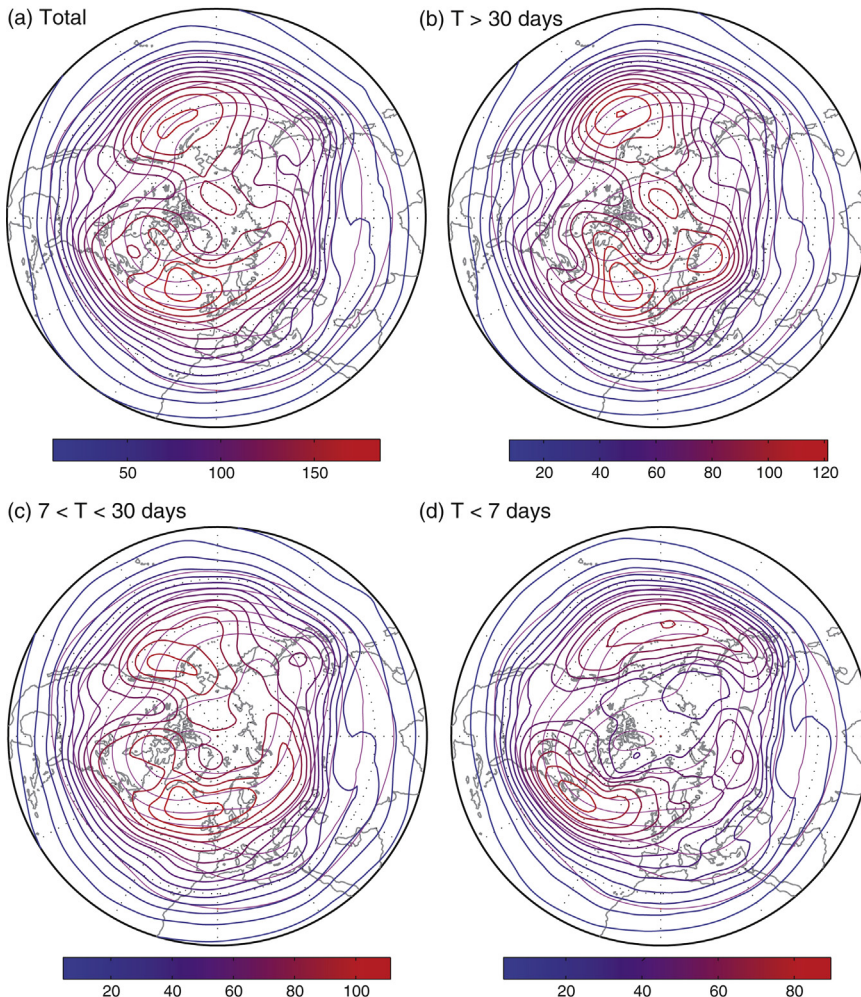


FIGURE 8.2 Standard deviation (STD, in meters) of 500 hPa height (blue-red contours and color bar) from its climatology for different time scales during the Northern Hemisphere winter half year (October to March). The climatology is shown as thin magenta contours. (a) Total STD of daily 12Z data, (b) STD of variability with periods longer than 30 days, (c) STD for periods between 7 and 30 days, and (d) STD for periods shorter than 7 days. The contour interval for the climatology is 100 m. The projection is polar stereographic starting at 20°N. Data from ERA Interim (1979–2013).

In the Southern Hemisphere during winter (Fig. 8.3), the variability is much more zonally symmetric (large at all longitudes around 60°S), but the variability is greatest upstream of the topographic barrier formed by the Andes Mountains and the Palmer Peninsula and smallest over the mountains. High frequency variability is greatest in a zonally elongated

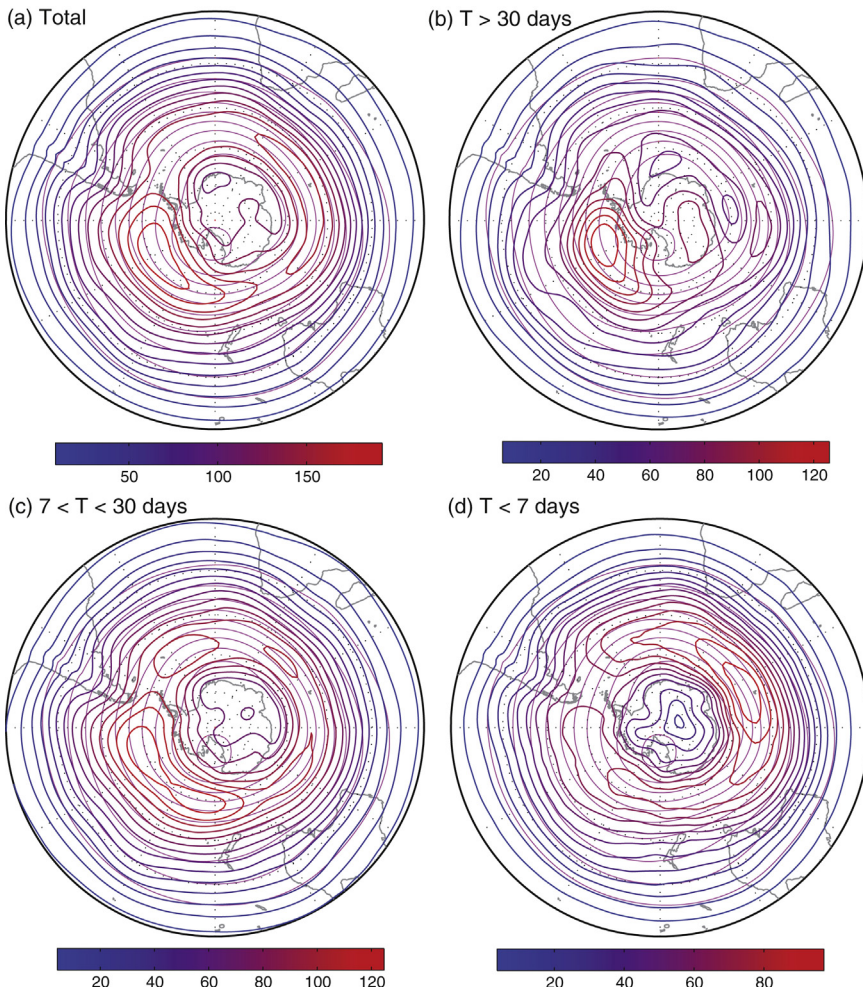


FIGURE 8.3 Same as Fig. 8.2, but for the Southern Hemisphere during its winter half year (April to September).

region peaking at about 50°S and 70°E in the Indian Ocean sector. The intermediate scale variability is largest downstream of this in the Pacific Sector between Australia and South America.

We can characterize the structure of the variability with one-point correlation maps of 500 hPa height anomalies. We choose a point where the variability of the time scale of interest is large, then correlate that point with all others. This reveals the characteristic spatial scale and structure of the variability with the time scale of interest.

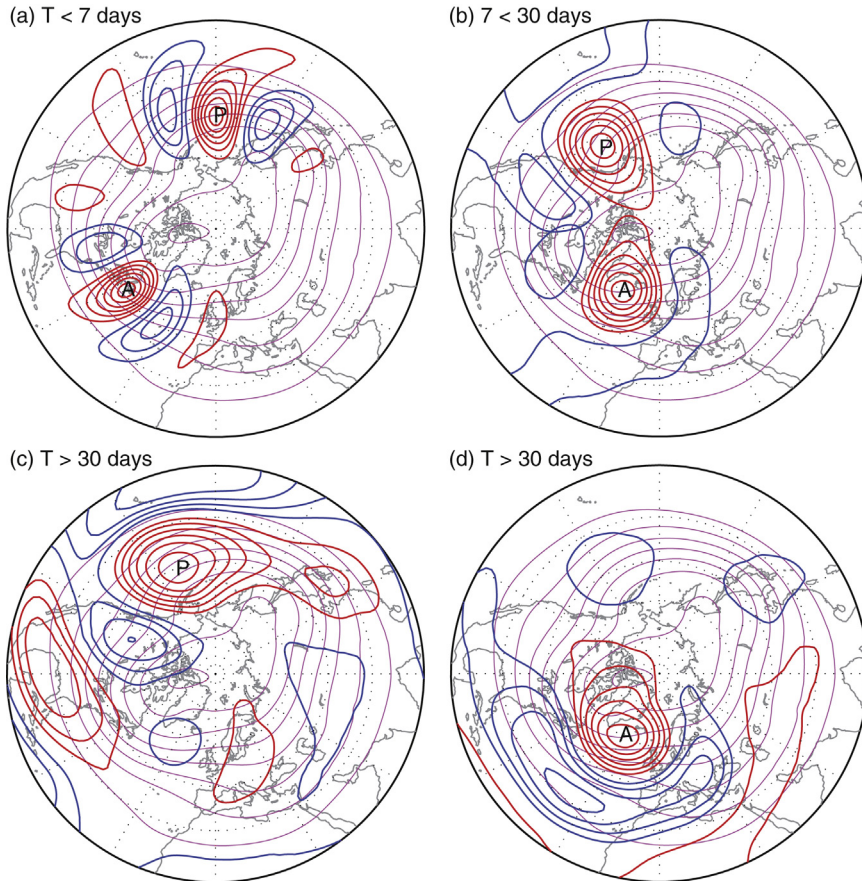


FIGURE 8.4 One-point correlation maps for the variability of the 500 hPa height on the time scales shown for the Northern Hemisphere during its winter season as in Fig. 8.2. The point where the letter is located is correlated with the rest of the hemisphere shown. Correlation patterns for two reference points are shown in (a) and (b) and only one in (c) and (d). Positive correlations are red contours, negative correlations are blue, the contour interval is 0.15 and the zero contour is not shown.

We begin by discussing the structures associated with the high-frequency variability in the Northern Hemisphere winter. One point was selected near the maximum of high-frequency variance in each ocean, and both one-point correlation maps are shown in Fig. 8.4a, along with the mean climatological height field. These are trains of waves with typical wavelengths of 50° of longitude (seven waves around a latitude circle or wavenumber 7). They occur near the troughs in the climatological height downstream of Asia and North America where the mean zonal westerlies

are strong. They tend to move eastward following the direction of the mean wind, but slower than the mean wind at 500 hPa.

In the Northern Hemisphere winter, the structures associated with 7–30 day variability are larger in spatial scale, however, they do not have such strong wavelike structure as the high-frequencies eddies, but appear mostly as blobs that represent localized up and down movement of the height surfaces without any strong connections to other regions. The variability with periods greater than 30 days does have some characteristic structure. A reference point in the mid-latitude Pacific Ocean captures a large-scale wave train following a great circle route from the western tropical Pacific to the Gulf of Mexico ([Fig. 8.4c](#)). It arises from natural variability of the atmosphere, but it is also strongly affected by tropical SST variations associated with El Niño events, as we shall see later. It appears here with the sign opposite to that associated with El Niño events, which produce a low pressure center in the North Pacific. A reference point in the North Atlantic shows a height correlation with a strong north–south dipole pattern. This is known as the North Atlantic Oscillation or NAO, and is the dominant mode of low-frequency variability in the North Atlantic. Note that it is elongated in the east–west direction forming a north–south dipole, whereas the high frequency wave trains are elongated in the north–south direction and form eastward propagating wave trains. These differences in structure can be related to linear wave theory and to the mechanisms by which these modes gain energy (Hoskins et al., 1983).

In the Southern Hemisphere during winter ([Fig. 8.5a](#)), we also see wave trains at high frequencies, and the ones with the largest variance are in the Indian Ocean sector where the high frequency variance is greatest. The scale of the wave train in the Indian Ocean sector is larger than that in the Pacific Ocean sector because the winds are stronger in the Indian Ocean. Because of the greater zonal symmetry and stronger zonal winds in the Southern Hemisphere, the intermediate scales also take the shape of east–west-oriented wave trains, but the zonal wavelengths are closer to 90° of longitude, so with a zonal wavenumber of 4 instead of 7 as for the high-frequency wave trains ([Fig. 8.5b](#)). If we choose a point near the center of the maximum height variability upstream of South America at 65°S, we also find a low-frequency pattern that looks like a wave train that appears to stretch from New Zealand to the subtropical Atlantic Ocean ([Fig. 8.5c](#)). A bit of north–south dipole is also mixed in with this Rossby wave train, as the heights equatorward of the center at 65°S are negatively correlated with it.

If we choose a reference point directly over the South Pole ([Fig. 8.5d](#)), then the correlation pattern has a strongly annular pattern with height anomalies of opposite sign at most all longitudes at about 45°S. It has a shape like a donut, with heights in mid-latitudes going up or down while the heights over the pole go down or up. This mode of variability is called the Southern Annular Mode, or SAM. It results from interactions

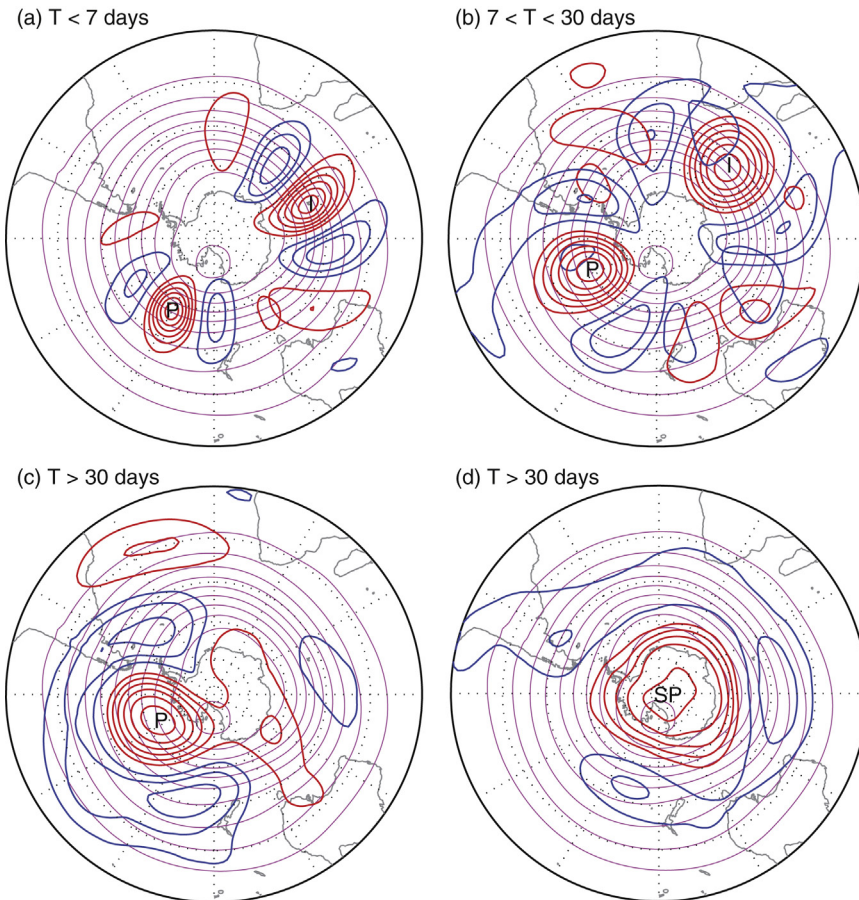


FIGURE 8.5 One-point correlation maps as in Fig. 8.4, except for the Southern Hemisphere in its winter half year of April through September.

between the high-frequency eddies and the zonal mean wind. SAM variability is internally generated, but it can be influenced by other things, and responds to forced climate change in global warming simulations.

Although most of the patterns in Figs 8.4 and 8.5 can be understood as trains of Rossby waves, the SAM is unusual in that the zonal-mean variation is dominant. To get another view of this mode of variability we can consider the EOFs of the daily zonal mean wind. The daily zonal mean wind is first computed, then the structures that explain the most variance of the daily zonal wind are computed, weighting by area and mass for the region from 20°S to 90°S and from 1000 hPa to 200 hPa, respectively. The first two such EOFs explain 40% and 21% of the variance thus constrained. Shown in Fig. 8.6 are the regressions of the zonal wind onto the first two

EOFs, so that the plots show the amplitude explained by typical variability of the EOF. The first EOF is equivalent to the Southern Annular Mode, and represents a north–south shifting of the eddy-driven mid-latitude jet (see Figs 6.4 and 6.16), whereas the second EOF represents a narrowing and broadening of the jet. The SAM is interesting in that it explains 40% of the variance, which is about twice that of the second EOF. Another special feature of SAM is that it not only explains a large amount of variance, but an even larger fraction of the variance at very low frequencies. For periods of 30 days or longer, the SAM explains 52% of the variance, whereas the second EOF explains only 22% and the third 8%.

The SAM anomalies are more persistent than those of the second EOF because the high-frequency eddies act to sustain jet shifts. High-frequency eddies propagate out of the jet, and as they do so they transport zonal momentum into the jet, thus sustaining it. The second EOF is not sustained by eddy interactions and its variations have less persistence. This is because, as the jet gets sharper, the eddies are less able to propagate away, so the momentum flux into the jet weakens as it gets sharper. The SAM is very interesting and important within the context of climate change. Its amplitude is large enough that it represents a shift in the latitude of the jet maximum of about 5° of latitude. In addition to its weather impacts, this shift is very important for wind stress driving of the ocean and sea ice. The SAM also appears to respond strongly to human forcing of the climate system, such as changes in the stratosphere due to ozone depletion, and models predict that the SAM will respond to global warming by moving the extratropical jet poleward.

8.2.2 Tropics: The Madden Julian Oscillation

In the tropics, convection releases latent energy that drives circulations with scales ranging from individual convective systems to global-scale circulations. Convection is organized both because convection moistens the atmosphere above the boundary layer and this encourages further convection, and also because convection drives large-scale motions that can supply moisture at low levels, supporting convection where it is occurring and suppressing it elsewhere. This can result in superclusters of intense convection or tropical cyclones, easterly waves, and global-scale tropical variability with time scales of a month or more.

In 1971, Roland Madden and Paul Julian discovered that tropical pressure and wind fields have a preferred mode of variability with a broad time scale centered around 40–50 days, but extending from 25 to 60 days. The Madden–Julian Oscillation (MJO) is strongest in the western Pacific and Indian Ocean regions during Northern Hemisphere winter, but occurs in all seasons and can be seen at all longitudes in the tropics, and also has effects in middle latitudes. It appears to result from a coupling between tropical convection and global-scale wind patterns near the equator. Its amplitude

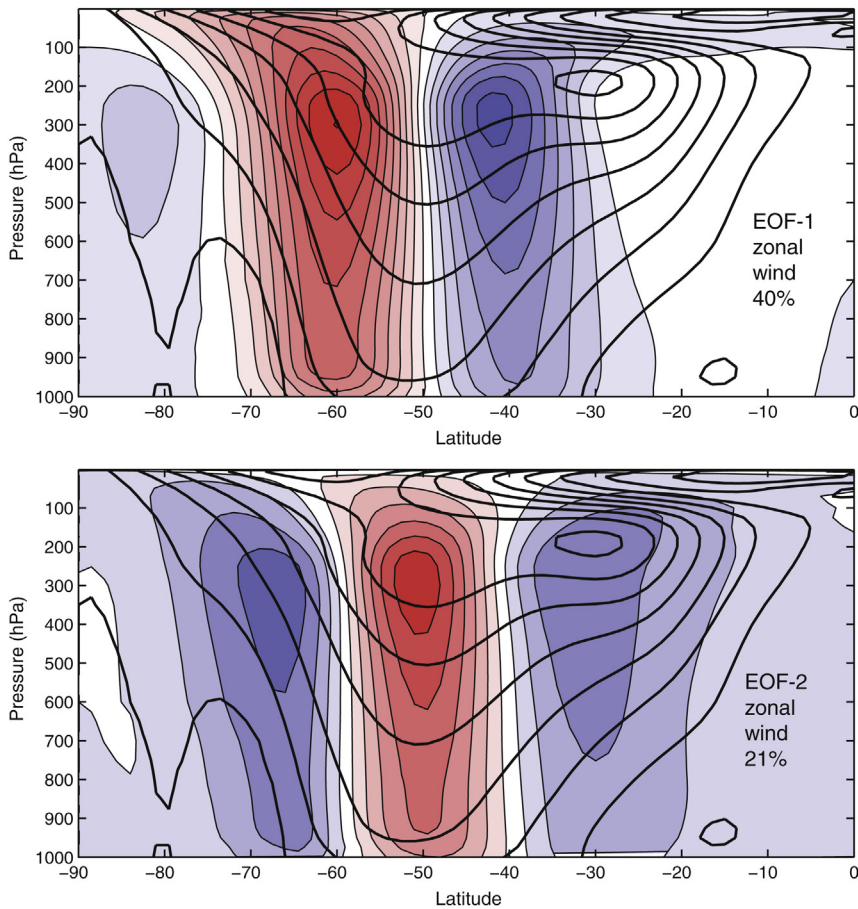


FIGURE 8.6 The first two EOFs for daily zonal mean wind variations in the Southern Hemisphere for all days of the year. These structures explain 40 and 21% of the area- and mass-weighted daily variance of the zonal mean wind between 20°S and 90°S, respectively. The heavy black contours are the zonal mean wind climatology for the annual average. Contour intervals for zonal mean wind are 5 ms^{-1} and contours for the EOFs are 0.5 ms^{-1} . Colors indicate the sign of the EOF anomaly. Top level is 1 hPa.

and persistence are sufficient to cause breaks in the Asian Summer Monsoon and transitions in the state of the tropical coupled ocean-atmosphere system (see ENSO below). It can also modulate the occurrence and intensity of tropical cyclones, typhoons and hurricanes (Fig. 8.6).

To give a sense of the time and space variability of the MJO, we average the OLR from 15°S to 15°N, filter it in time to remove variations with time scales longer than 90 days and shorter than 15 days, and plot it as a function of time (Fig. 8.7). Two representative year-long periods are shown starting on July 1 and ending on July 1 the following year. Negative anomalies

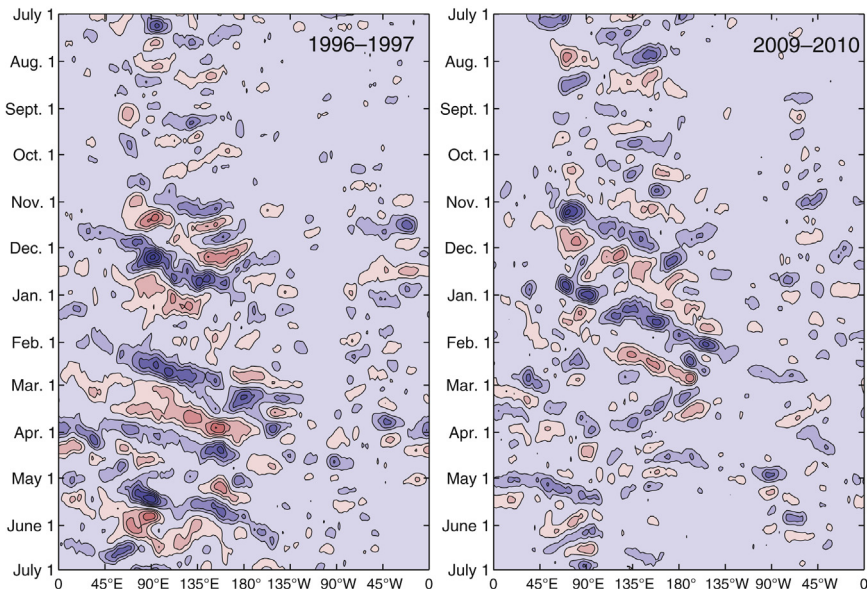


FIGURE 8.7 Longitude–time plots of band-pass filtered tropical OLR anomalies for 1996–1997 and 2009–2010. OLR is averaged from 15°S–15°N and periods longer than 90 days and shorter than 15 days have been filtered out. Blue shading is negative, the contour interval is 10 W m^{-2} , and the zero contour is not shown. OLR data from Liebmann and Smith (1996).

(blue shading) indicate enhanced cloudiness and precipitation. The largest anomalies are $\pm 40 \text{ W m}^{-2}$ – quite large. From these examples we can see several features of the MJO. It is strongest in the Northern Hemisphere winter half year. It is intermittent and does not have a fixed period, but large amplitude variations in OLR occur with characteristic time scales that are longer than a month. The anomalies often move from west to east, starting in the Indian Ocean region and weakening in the central Pacific Ocean. Some other phenomena can be seen that propagate westward with shorter periods.

Wheeler and Hendon (2004) suggested an index of the MJO that is based on the EOFs of OLR and zonal wind at 200 hPa and 850 hPa, all averaged over the latitude band from 15°S to 15°N. Here we remove all variability with time scales longer than 90 days to remove the seasonal and El Niño signatures, then compute the joint EOFs of zonal wind at 200 and 850 hPa. This produces two leading EOFs that explain 20 and 16% of the combined variance of the 200 and 850 hPa zonal wind fields. Then we project these EOF structures onto the original data to compute the daily time series of the amplitudes of these two leading EOFs. These time series are highly coherent with each other at periods between 90 and about 25 days, with the first EOF preceding the second EOF by several weeks. Thus the first two EOFs are expressing a single phenomenon, the eastward moving MJO seen in Fig. 8.7. To show the full structure of the MJO, we take the time

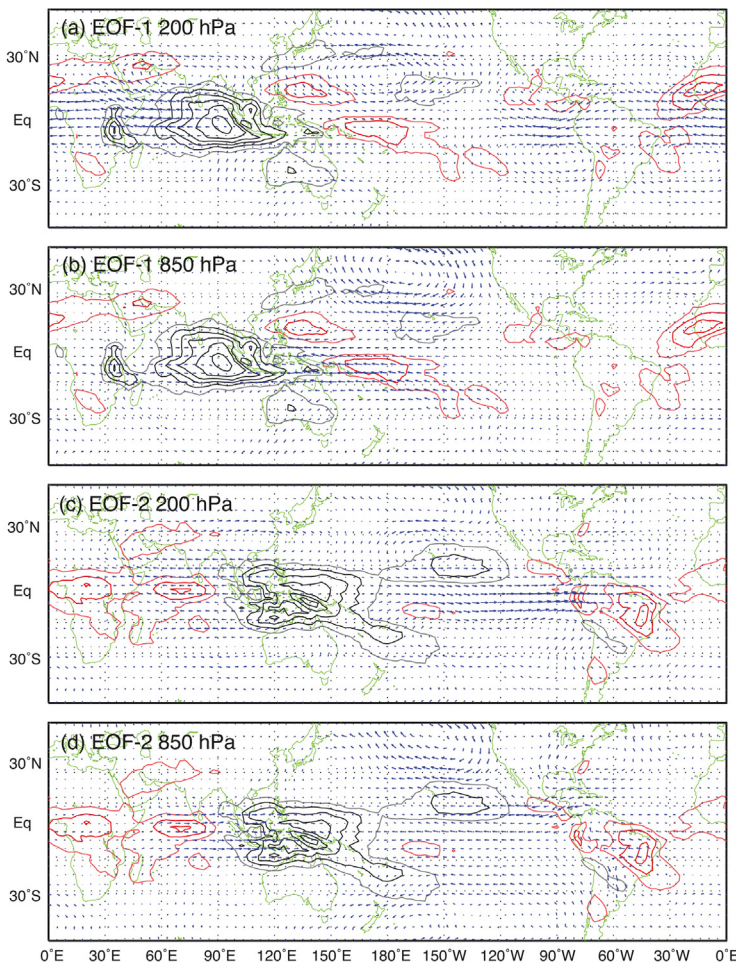


FIGURE 8.8 Wind vector and OLR regressions associated with the First and Second EOFs of 200 hPa and 850 hPa zonal wind during the Northern Hemisphere Winter Half year. Contour interval for OLR is 2 W m^{-2} and the zero contour is not shown. Black contours indicate high clouds and precipitation.

series of the amplitude of these two EOFs and regress them onto the OLR and the wind vectors at 200 and 850 hPa. The result is shown in Fig. 8.8.

The top two panels of Fig. 8.8 show the regressions of the wind vectors and the OLR onto the first EOF. This EOF has a large negative OLR anomaly centered at about 90°E in the Indian Ocean, indicating strong convection and precipitation there. This OLR anomaly is associated with easterly 850 hPa wind anomalies near the equator extending to the east as far as the central Pacific, and westerly anomalies extending west to the African coast. The low-level winds are thus converging where the precipitation is occurring. At 200 hPa, strong easterly wind anomalies extend westward

from the region of low OLR and convection. The wind anomalies thus have a strong vertical shear, being westerly near the surface and easterly near the tropopause over the Indian Ocean. At the time of the oscillation represented by EOF-1, a strong anticyclonic wind circulation appears in the North Pacific, centered at about 40°N , just east of the Dateline and most obvious at 850 hPa. The MJO thus has a coherent effect on the mid-latitude circulation during the winter season. The MJO heating anomaly interacts with the subtropical jet stream in the western Pacific to produce this extratropical wave anomaly.

The bottom two panels of Fig. 8.8 showing EOF-2 are similar in many ways to the top panels except that the negative OLR anomaly has shifted to the east and is now centered over Indonesia and the western Pacific, with a convection anomaly extending down the South Pacific Convergence Zone. These two EOFs together represent the eastward propagation of a global-scale wind and precipitation anomaly. At the later stage represented by EOF-2, westerly wind anomalies at 850 hPa extend toward the west over the Indian Ocean to Africa with easterly anomalies above at 200 hPa in the same region. Low-level easterly anomalies and high-level westerly anomalies extend from the convection over Indonesia all the way across the Pacific to South America, so that the wind anomalies on the equator are near global in extent.

8.3 EL NIÑO, LA NIÑA, AND THE SOUTHERN OSCILLATION

The El Niño-Southern Oscillation phenomenon (ENSO) is a coupled mode of variability of the tropical ocean-atmosphere system centered in the Pacific Ocean sector, but coupled to global weather patterns. The El Niño nomenclature comes from the warm sea surface temperatures (SST) phase of ENSO appearing at the west coast of South America around Christmas time. La Niña was introduced as a convenient nomenclature for the cold phase, or feminine side, of ENSO. Southern Oscillation refers to the associated patterns in surface pressure that were discovered by Sir Gilbert Walker in the 1920s (Horel and Wallace, 1981).

To understand the genesis of the ENSO phenomenon, we need to consider the climatology of the coupled ocean-atmosphere system along the equator in the Pacific Ocean sector. Figure 8.9 shows the atmospheric vertical velocity and the oceanic potential temperature along the equator. To understand ENSO, we focus on the Pacific Ocean. The thermocline slopes downward toward the west, with a deep, warm mixed layer in the western Pacific and a shallow mixed layer and shallow thermocline in the east. This sloping thermocline is maintained in large measure by the easterly wind stress on the tropical Pacific Ocean, indicated by the large black arrow in Fig. 8.9. The strength of the easterlies is enhanced in the Pacific by the upward motion

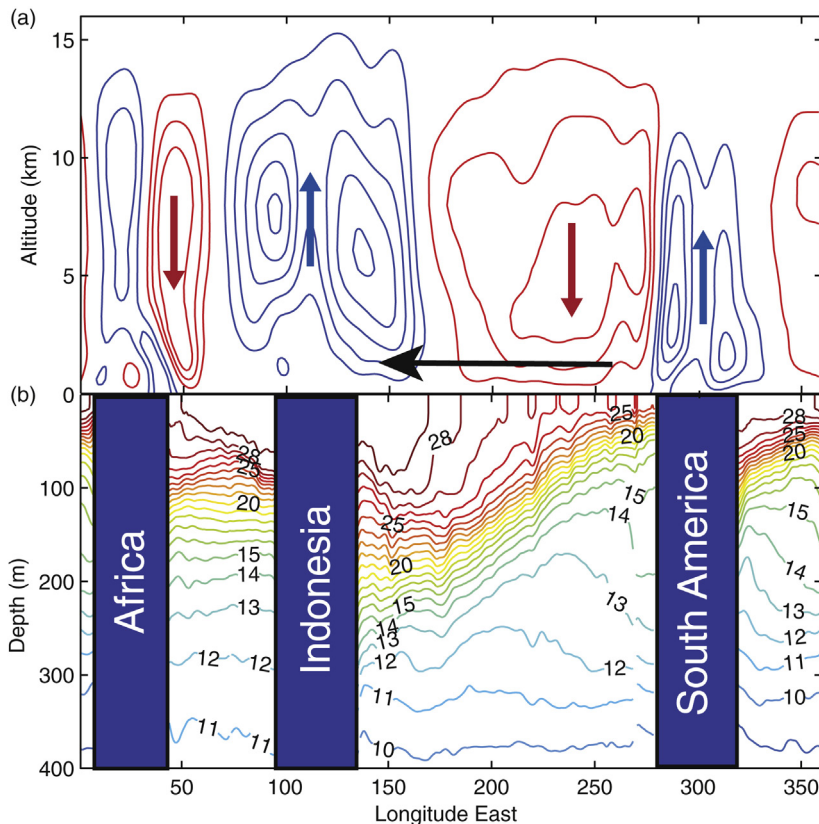


FIGURE 8.9 Atmospheric vertical velocity (a) and oceanic potential temperature (b) along the equator. Vertical arrows indicate direction of vertical motion, black horizontal arrow indicates direction of surface winds over the Pacific Ocean.

driven by convection over Indonesia, balanced by the downward motion supported by radiative cooling east of the dateline, where convection is much less probable. One thus sees an immediate connection between the preference for convection to occur in the far west Pacific and the easterlies that drive the westward SST and thermocline depth gradients. The positive feedback between warm SST in the west and cool in the east that drive easterlies that drive cool SST in the east and warm in the west is called “Bjerknes feedback.” If these easterlies weaken, then pressure forces would begin to flatten the thermocline and warm surface water would flow toward the eastern Pacific. This would make precipitation more likely to form over the warmed SST in the eastern Pacific and the easterly winds would further weaken. This is the basic idea behind the warm ENSO, or El Niño event, which employs the Bjerknes feedback in reverse.

Figure 8.10 is a schematic diagram showing La Niña, Normal, and El Niño conditions along the equator in the tropical Pacific. The coupled

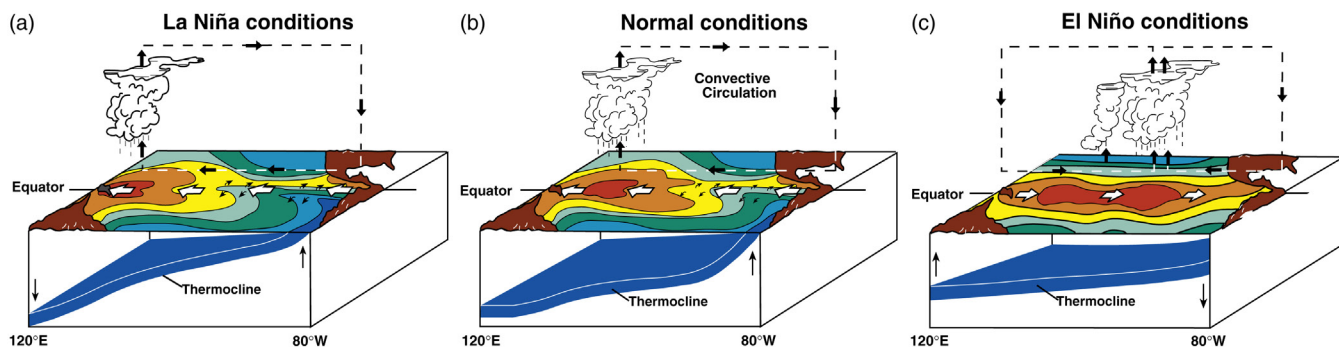


FIGURE 8.10 Schematic diagram showing the atmospheric and oceanic conditions along the equator in (a) La Niña, (b) Normal, and (c) El Niño conditions. NOAA/PMEL TAO Project.

system has a lot of available potential energy when the thermocline is steeply sloped, as during La Niña conditions, and an instability can occur then that leads to a rapid and sustained warming of the eastern Pacific with attendant shifts in the precipitation and associated atmospheric circulation patterns. La Niña occurs when the convection is farther west, the thermocline slope is great and the SSTs are cold in the central and eastern Pacific. El Niño is the opposite with rainfall in the central and eastern Pacific and relatively flatter SST and thermocline across the Pacific from west to east. When the convection is farther east, the easterly trade winds weaken and this suppresses the upwelling in the east that normally sustains the sloping thermocline.

The state of ENSO is well characterized by the SST along the equator. [Figure 8.11](#) shows the monthly mean SST averaged between 5°S and 5°N from 1886 to 2013. The mean annual cycle has been removed, but the long-term trend is visible by comparing the early years with the latest years. Particularly large warm events occurred in 1982–1983 and 1997–1998. The largest SST anomalies occur from the coast of South America (~80°W) to the dateline (180°W). Sometimes the SST anomalies emerge first at the coast of South America (e.g., 1966 and 1973) and sometimes they emerge first farther offshore (e.g., 1982 and 1992). Some smaller SST anomalies occur in the Atlantic Ocean and to an even lesser extent in the Indian Ocean.

The characteristic time scale of the ENSO cycle can be estimated from the power spectrum of the SST anomaly averaged over the region from 5°S to 5°N and from 90°W to 150°W. This is often called the Niño-3 index of the state of ENSO. The power spectrum in [Fig. 8.12](#) shows that the strongest variability is at periods from 3 to 5 years, but that significant variability extends across periods from 2 to 20 years.

One of the principal effects of the changed SST on the atmosphere is to move the precipitation in the tropics, which tends to locate over the warmest SST. [Figure 8.13](#) shows the regression of the outgoing longwave radiation (OLR) anomalies onto the Niño-3 index of tropical SST. When the SST in the equatorial East Pacific is anomalously warm, the convection is enhanced in the central and eastern Pacific and decreased over Indonesia and Australia. The anomalies in tropical convection are to the west of the largest SST anomalies because the SST generally increases from east to west and the response of convection to a given SST anomaly is greater over warmer water. The dipole pattern of OLR anomaly represents an eastward movement of the main convection region in the far western Pacific. Although the OLR time series begins in the middle of 1974 and is therefore rather short, it does show some of the consistent impacts of El Niño on tropical precipitation. During November to March El Niño can mean dry conditions over Indonesia and Australia and also north-east South America, but wet over the Gulf of Mexico. During the May to September season El Niño can also mean reduced summer monsoon

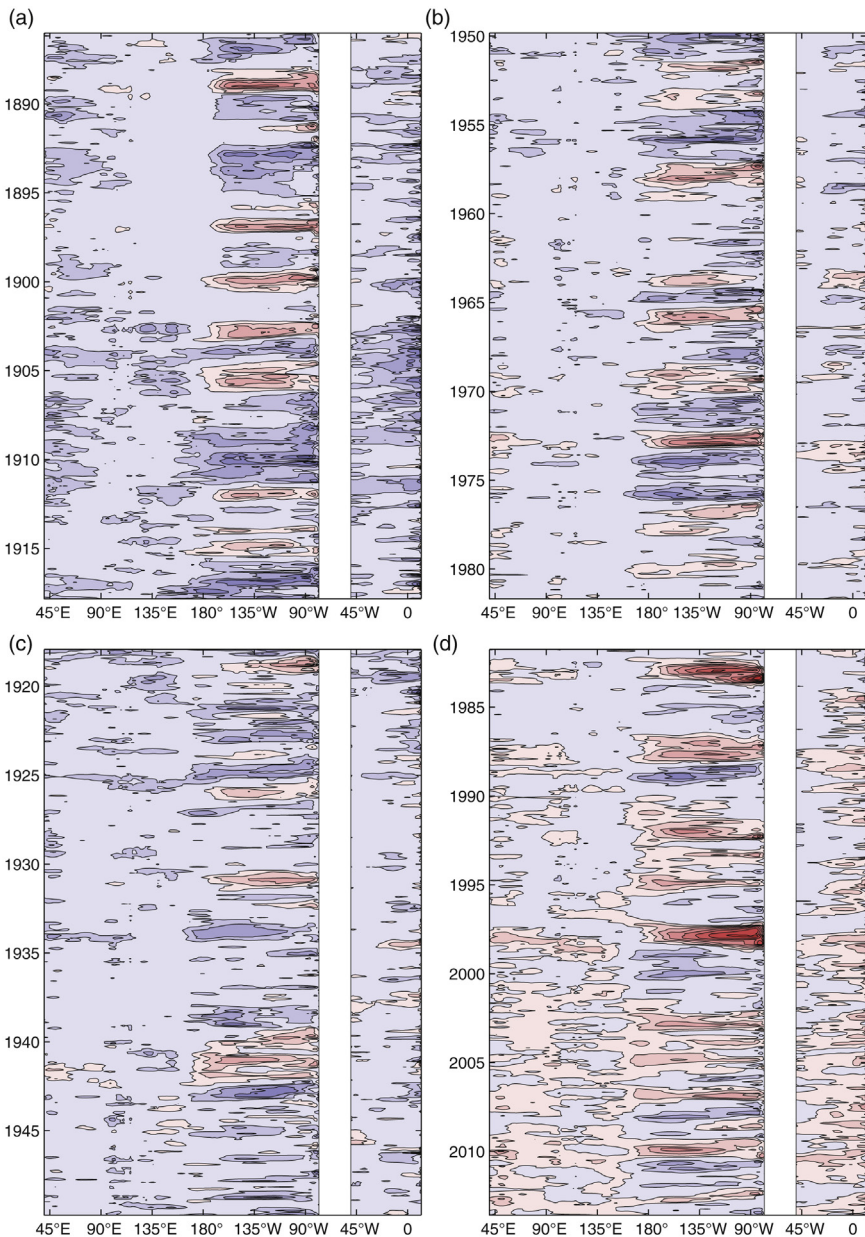


FIGURE 8.11 Monthly SST anomalies averaged over 5°S–5°N as a function of longitude and time since 1886. Year increases downward in each panel. The contour interval is 0.5°C and positive anomalies are shaded red. The mean annual cycle has been removed, but the long-term trend is included. The blank area is the land area of Central America. The land area of Africa is not shown. *Data are from the NOAA ERSST data set.*

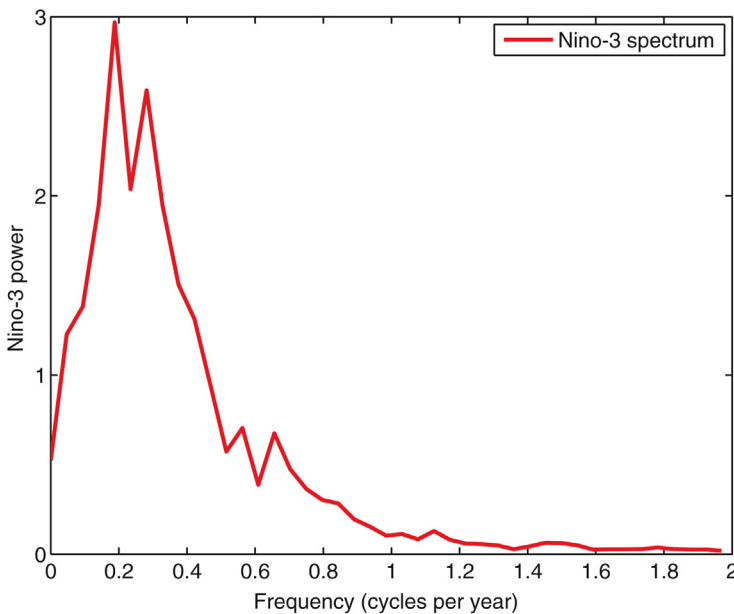


FIGURE 8.12 Power spectrum of the Niño-3 index, the anomalies of SST averaged over 5°S to 5°N and 90°W to 150°W. The linear trend was removed before computing the spectrum from the monthly data from 1886 to 2013. The period is just the inverse of the frequency in cycles per year, so 0.2 cycles per year correspond to a period of 5 years. The greatest variance is associated with periods between 3 and 5 years. *Data from the NOAA ERSST data set.*

precipitation in India. Another impact is precipitation reaching the west coast of equatorial South America, where the SST anomalies also have an impact on fisheries.

The extratropical response to ENSO can be assessed by regressing the Niño-3 index of tropical SST into the global field of 500 hPa height. Because of the low-frequency and episodic nature of ENSO variations, we need a long record to get robust results. Here we turn to the Twentieth Century Reanalysis product, which goes back to 1871 (Compo et al., 2011). The 500 hPa field in this reanalysis is mostly a model-calculated response to SST and surface-pressure observations, although it closely resembles the reanalysis products that assimilate all modern observations. We use monthly mean observations to construct the regression patterns shown in Fig. 8.14 for the Northern Hemisphere winter (November to March) and the Southern Hemisphere winter (May to September). The basic patterns are not sensitive to the exact choice of winter half year. Note that the sign is for El Niño conditions with a warm tropical East Pacific Ocean, but would be reversed for La Niña. The entire tropical troposphere warms up

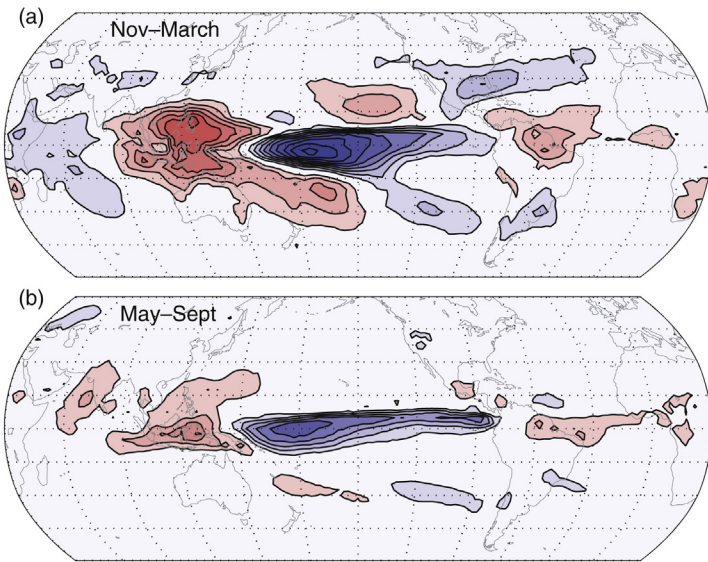


FIGURE 8.13 Regression of monthly OLR anomalies with the Niño-3 index of SST for the November to March (a) and May to September (b) seasons. Contour interval is 2 W m^{-2} , the zero contour is not shown. Negative values are shaded blue and indicate reduced OLR, enhanced high cloud and increased precipitation. Based on NOAA interpolated OLR from June 1974 to 2013.

during an El Niño, so that the 500 hPa height increases everywhere in the tropics from about 20°S to 20°N . This strengthens the subtropical winds a bit and moves them toward the equator. The opposite happens during La Niña.

The response of the extratropical atmosphere to ENSO depends on the anomalies in heating produced as the precipitation shifts to follow the warmest SST values (Fig. 8.13) and the interaction of this anomalous heating with the mean wind fields (Sardeshmukh and Hoskins, 1988). In the November–March season, the extratropical response is somewhat symmetric about the equator, with similar responses in the Northern and Southern Hemispheres. Note the similarity of the November–March pattern with the one-point correlation map in Fig. 8.4c, although it is shown with opposite sign there. Even though the heating anomalies are displaced somewhat into the Southern Hemisphere, the strong subtropical jet in the Northern Hemisphere winter is quite responsive to the heating anomalies so that a nearly symmetric response is generated. The wave forced in the tropics propagates poleward and eastward along a great circle route and interacts with the mean wind and eddies along the way. This downstream wave effect has much significance for North America, as a warm event generates a low over the North Pacific, a high over western North America

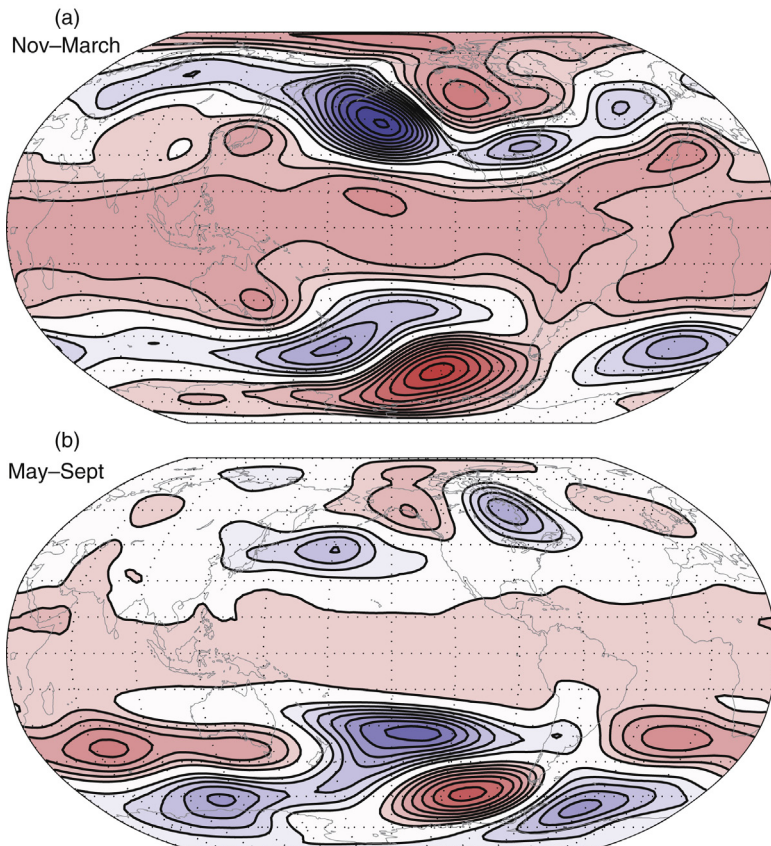


FIGURE 8.14 Regression of monthly 500 hPa height anomalies with the Niño-3 Index of SST for November to March (a) and May to September (b) seasons. Contour interval is 2 m, the zero contour is not shown and positive values are shaded red. Based on NOAA Twentieth Century Reanalysis and NOAA Extended SST data sets from 1871 to 2013.

and a low over the South East USA. These anomalies are associated with important weather impacts of El Niño, including warmth over western Canada and Alaska, stronger winter storms in Southern California and cooler and wetter conditions in the South East USA.

The response during the May–September season is very different in the Northern Hemisphere because the mean winds are very different and the tropical convection is moved off the equator during summer in association with the Asian Summer Monsoon (Fig. 5.4). The OLR anomalies are slightly smaller during the May to September season and their Northern Hemisphere impact is rather weak, but their influence on the Southern Hemisphere is still strong.

8.4 DECADAL VARIATIONS OF WEATHER AND CLIMATE

Although instrumental climate records are short for defining variations with time scales of decades or longer, it is clear that such variability must exist, perhaps mostly because of the ocean. Decadal time scales are also challenging because on this time scale the natural variability of the climate system becomes difficult to separate from the human influences that have become steadily stronger during the period of instrumental records. Methods are available that may be able to distinguish natural and anthropogenic changes in the observations, but whether they have worked or not is often a judgment call. Methods using climate models with and without human influences can be used to unambiguously separate natural variability from human influences, and these will be discussed in Chapter 13.

Global maps of SST can be used to investigate decadal variability. Global analyses of SST start as early as 1854, but the earlier records are based on extrapolation from relatively sparse data, so that the more recent years are more reliable. To search for natural variability on decadal time scales, we can first start by removing annual cycle and the global mean SST from monthly mean data. Removing the global mean from each month may have the effect of removing global mean trends associated with both the human influence and with globally coherent changes in the observing system. Therefore, we hope that what is left to investigate is the spatial structure of internal climate variability.

One objective way of searching for important patterns in SST variability is EOF analysis. For example, if we start with monthly anomalies of SST over the globe, then the first pattern that comes out is ENSO, and it explains about 17% of the global SST variance, much more than any other mode of variability. [Figure 8.15](#) shows the SST anomaly structure associated with the first EOF of global SST along with its amplitude time series since 1880. The spatial structure is characterized by a large warm anomaly along the equator in the eastern Pacific Ocean and cold anomalies in mid-latitudes of each hemisphere. The extratropical anomalies are caused by the Rossby wave response to the tropical heating anomalies shown in [Fig. 8.14](#). The low pressure centers at around 40° latitude at 150°W in each hemisphere drive cooling of the ocean surface there, mostly during the winter season. This remote forcing of the extratropical SST by waves generated by tropical heating anomalies associated with ENSO has been called the “atmospheric bridge” (Alexander et al., 2002).

The time series of the global ENSO mode ([Fig. 8.15b](#)) shows strong variability on time scales of 2–6 years consistent with the power spectrum of the Niño-3 index shown in [Fig. 8.12](#). One can clearly see the strong warm ENSO (El Niño) events in 1998 and 1982, during which the anomalies in SST were about three times the magnitudes shown in [Fig. 8.15a](#). Since

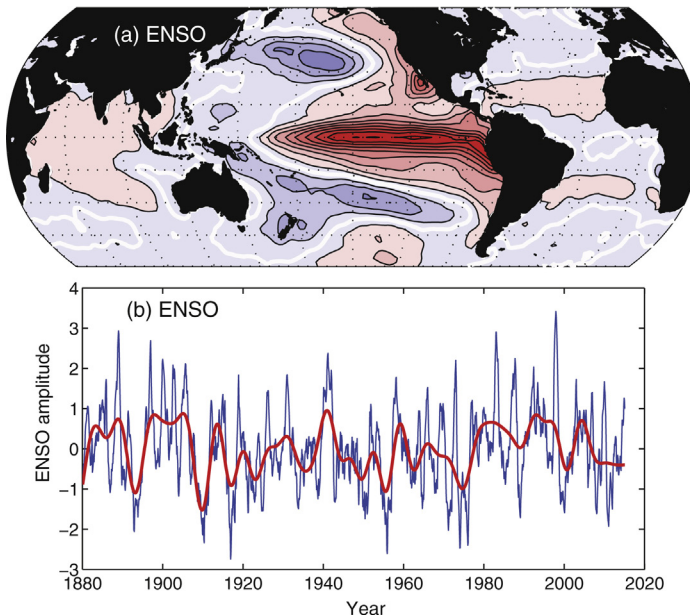


FIGURE 8.15 The structure of El Niño. (a) The spatial pattern of ENSO; the regression of monthly SST onto the first EOF of global SST from 1880 through January 2015. Contour interval is 0.1 K, positive anomalies are red and the zero contour is in white. (b) The time structure of ENSO; time series of the amplitude of the spatial pattern in units of standard deviations. The red line is smoothed to remove periods shorter than six years.

1998, the ENSO mode has been mostly negative, indicating colder than normal SST in the equatorial east Pacific. In addition to the 2–6 year time scale of the life cycle of ENSO, one can also see longer period variations in the ENSO mode. These are highlighted by the smooth line in Fig. 8.15b, which has filtered out variations with periods shorter than 6 years. Because ENSO is such a dominant mode of interannual variability, these decadal variations in ENSO can have a significant global influence.

The Pacific Decadal Oscillation (PDO) and the Atlantic Multidecadal Oscillation (AMO) are often discussed. To isolate these we can perform the EOF analysis as above for ENSO, but instead of including the global ocean, consider only the North Pacific and North Atlantic. The PDO was first defined as the dominant EOF of SST north of 20°N in the Pacific (Mantua et al., 1997). This structure and its time series are shown in Fig. 8.16. The PDO looks very much like ENSO, with a bit more emphasis on the extratropical signal and longer time scales. It can be argued that the PDO is nothing more than the low-frequency component of ENSO, and it can be seen that the time series of ENSO and PDO are correlated.

The AMO was first characterized as the anomalies in the areal mean temperature of the North Atlantic (Schlesinger and Ramankutty, 1994).

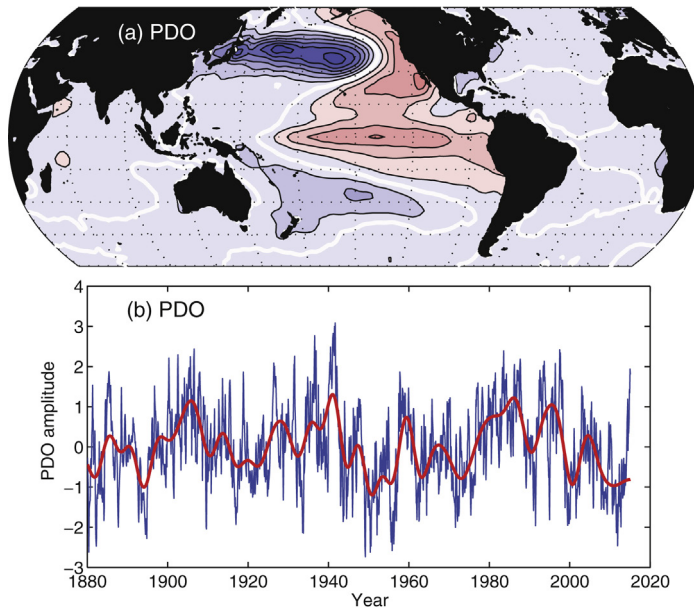


FIGURE 8.16 The structure of the PDO. (a) The spatial pattern of the PDO; the regression of monthly SST onto the first EOF of SST north of 20°N in the Pacific from 1880 through January 2015. Contour interval is 0.1 K, positive anomalies are red and the zero contour is in white. (b) The time structure of the PDO; time series of the amplitude of the spatial pattern in units of standard deviations.

Figure 8.17 shows the first EOF of monthly SST anomalies for the Atlantic Ocean north of 20°S. It consists of two centers of positive SST anomaly in the subtropics west of Africa and in the extratropics east of Newfoundland. The time series of this mode shows very strong decadal variations, with a very interesting transition from negative anomalies in the mid-1970s to the late 1990s toward positive anomalies in the late 1990s to 2015, the latest time shown in Fig. 8.17.

The time series of the amplitudes of the PDO and the AMO can be regressed against anomalies in the Northern Hemisphere 500 hPa height field in winter to show how these patterns relate to meteorology (Fig. 8.18). The 500 hPa height anomaly pattern associated with the PDO is very similar to the response to ENSO (Fig. 8.14) and to the one-point correlation map in Fig. 8.4c. It is the wintertime extratropical response to El Niño. The low pressure over the North Pacific and the associated stronger winds and colder temperatures drive the cool SST anomaly in the North Pacific.

The height anomaly associated with the AMO is a north–south dipole in the North Atlantic that resembles the one-point correlation map of low-frequency variability in Fig. 8.4d, often called the North Atlantic Oscillation. The high-pressure center to the north is associated with weakened

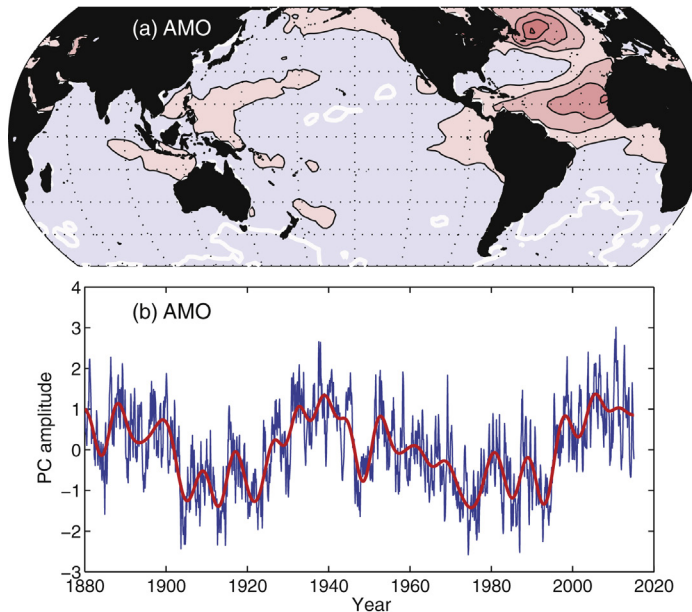


FIGURE 8.17 The structure of the AMO. (a) The spatial pattern of the AMO; the regression of monthly SST onto the first EOF of SST north of 20°S in the Atlantic Ocean from 1880 through January 2015. Contour interval is 0.1 K, positive anomalies are red and the zero contour is in white. (b) The time structure of the AMO; time series of the amplitude of the spatial pattern in units of standard deviations.

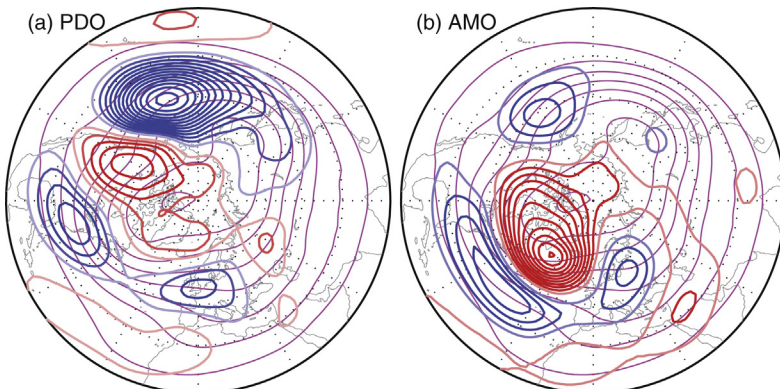


FIGURE 8.18 Regression of the 500 hPa height anomalies from the Twentieth Century Reanalysis onto the time series of the (a) PDO and (b) AMO time series during the November through March season. Contour interval is 3 m, positive contours are red. Thin magenta contours indicate the seasonal mean height field. Polar stereographic projection.

winds that generate a positive SST anomaly through reduced sensible heat exchange in winter. To understand how the low anomaly to the south in the AMO pattern ([Fig. 8.17b](#)) is associated with warm SST anomalies, one must remember that the winds in the subtropics during winter are easterly in the mean (Fig. 6.19). Therefore the westerly anomalies to the south of the low in [Fig. 8.18b](#) act to offset the climatological easterlies there and result in a net reduction of wind speed. This helps to suppress evaporative cooling there and contributes to the warm SST anomaly in [Fig. 8.17a](#).

The strong variability in the PDO and AMO at time scales of a decade or longer make them very interesting, in part because they may help to define the amplitude or structure of temperature change on time scales similar to the onset of human-induced warming. They have decadal time scales presumably because they interact with the ocean, especially in the extratropics where both ocean wave propagation and ocean heat storage possess inherently long time scales. During the winter when the mixed layer is deep, weather anomalies can lay down ocean temperature changes that are buried under the shallow summer thermocline (Figs 7.5 and 7.6) and then reemerge the next winter, giving ocean memory from one winter to the next. It is hoped that with greater understanding, and better data and data assimilation systems, we may be able to use climate models to make useful forecasts of some aspects of the natural variability of weather or climate, perhaps as much as a decade into the future, by using the initial state of the coupled atmosphere–ocean–land system.

EXERCISES

1. Compare the longitude of the maximum in high-frequency eddy variance ($T < 7$ days) with the longitude of the maxima in intermediate frequency variance ($7 < T < 30$ days) in [Fig. 8.2](#). Are your results consistent for the Atlantic and Pacific ocean regions?
2. The low-frequency variability in the Southern Hemisphere in [Fig. 8.3](#) is centered upstream of the Palmer Peninsula that juts out from Antarctica toward South America. Can you think of any reasons why this might be the case? How do you think this might influence the variability of sea ice in the Ross, Amundsen, and Bellingshausen seas in that region?
3. The Northern Hemisphere has two wintertime storm tracks, one over the Pacific Ocean and one over the Atlantic Ocean, but the Southern Hemisphere has only one long one centered in the southern Indian Ocean. Why do you think this is the case?
4. [Figures 8.4 and 8.5](#) indicate that the spatial scale of disturbances get larger as the time scale gets longer. Do you know why?

5. [Figure 8.6](#) indicates that a north–south migration of the Southern Hemisphere extratropical jet explains more of the variance of zonal wind than the sharpening or broadening of the jet. Can you explain why?
 6. [Figure 8.7](#) shows that the OLR anomalies associated with the Madden–Julian oscillation are strongest in the tropical Indian and Western Pacific regions, but the wind anomalies extend to other longitudes and into the extratropics. Can you explain why?
 7. Looking at [Fig. 8.9](#) it is apparent that a strong temperature gradient exists from east to west below the surface. If warm temperature is associated with less dense water, what would you expect the pressure gradient to be 150 m below the surface? What direction would the water at 150 m deep move if there was no wind stress being applied at the surface?
 8. Compare and contrast the OLR anomalies associated with ENSO in [Fig. 8.13](#) with those associated with the MJO in [Fig. 8.7](#). It has been argued that a big MJO event can be a precursor to a warm ENSO event. Can you explain why?
 9. Theory says that tropical heating anomalies generate Rossby waves near the equator that follow great circle routes as they propagate into the extratropics during winter. Can you connect the centers of the anomalies in [Fig. 8.14](#) and trace out the paths along which eddy energy must be propagating?
 10. Assemble a list of arguments for and against the following statement. “The PDO is just the low-frequency, extratropical signature of ENSO, nothing more.”
-